

Thermal emission modulation of fabrication-friendly, free-form metasurfaces via explainable deep-learning Bayesian optimization

Cite as: Appl. Phys. Lett. **126**, 051703 (2025); doi: [10.1063/5.0250273](https://doi.org/10.1063/5.0250273)

Submitted: 23 November 2024 · Accepted: 20 January 2025 ·

Published Online: 3 February 2025



View Online



Export Citation



CrossMark

Jintao Chen,¹ Zihan Zhang,² Zhequn Huang,³ and Kehang Cui^{4,a)}

AFFILIATIONS

¹School of Electronic Information and Electrical Engineering, Shanghai Jiao Tong University, Shanghai 200240, China

²School of Mathematical Science, Shanghai Jiao Tong University, Shanghai 200240, China

³Zhiyuan Innovative Research Center, Shanghai Jiao Tong University, Shanghai 200240, China

⁴School of Materials Science and Engineering, Shanghai Jiao Tong University, Shanghai 200240, China

^{a)}Author to whom correspondence should be addressed: cuikeheng@sjtu.edu.cn

ABSTRACT

Free-form metasurfaces with superimposed transformative meta-atoms provide a versatile platform to realize cross-band thermal emission control. However, design and manufacturing of free-form metasurfaces is extremely challenging, owing to the complex and fractal sub-wavelength topology. Here, we address these two issues by proposing an explainable deep-learning Bayesian optimization (DeepBO) framework to realize a library of fabrication-friendly, free-form metasurfaces with different light-matter interaction bandwidths. The DeepBO requires only 50 training data and is capable of screening high-dimensional design space of 10^{43} thermal photonic structure candidates with bandwidths from 0.3 to 3.2 eV. We unfold the black-box of deep-learning process by pattern recognition and identify the sub-space key features in the high-dimensional design space, which provides insights for thermal photonic metasurface design. We showcase the design and manufacturing of the broadband solar absorber and the narrowband thermophotovoltaic emitter with record-high spectral efficiency. The spectral selectivity of the fabricated free-form metasurface matches well with the design. The fabrication-friendly, free-form metasurfaces realized in this work can be generalized to thermal emitters for broad-ranges applications in energy and sensing.

Published under an exclusive license by AIP Publishing. <https://doi.org/10.1063/5.0250273>

08 February 2025 06:50:31

Thermal photonics is an emerging field^{1–5} of controlling thermal radiation in terms of spectrum (temporal coherence), directivity (spatial coherence), and polarization, which has great potential to enable advances in chemical fingerprinting,^{6–10} thermal imaging,^{11–13} radiative computing,^{14–16} infrared camouflaging,^{17–21} and thermophotovoltaic (TPV) conversion.^{22–25} Solar TPV (STPV) devices convert broadband solar irradiation to narrowband near infrared thermal emission which matches the electronic bandgaps of photovoltaic (PV) cells. By harvesting sub-bandgap photons and hot carriers, TPVs can exceed the Shockley–Queisser (SQ) efficiency limit with high output energy density. The defining figures of merit for STPV include the solar-thermal conversion efficiency,²⁶ quality factor,²⁷ spectral efficiency,²⁸ etc., which are extremely sensitive to the spectral selectivity. A slight spectral mismatch may cause severe performance degradation. Precise control of thermal radiation over broad wavelength range is the key to realize high power conversion efficiency in STPV.

High-dimensional free-form metasurfaces with superimposed meta-atom resonators offer an opportunity for broadband spectral control. However, fundamental challenges remain in the design and manufacturing of high-dimensional free-form metasurfaces. First, the design of high-dimensional metasurface is mathematically challenging for Maxwell solvers. Tremendous efforts have been invested on neural network (NN) approximators and machine learning algorithms to accelerate the design. Nevertheless, the training of NN is extremely data intensive and lack of generality for thermal photonic metasurfaces. Algorithms such as transfer learning,^{29–31} ensemble learning,³² and meta-learning^{33,34} have been proposed to increase the generality of deep learning. However, the transferability of the trained NN remains a black-box process without global understanding of the design space and physics insights of the high-dimensional complex metasurfaces. Moreover, deep-learning framework discretizes the meta-atom into pixels or voxels with fixed geometries for use as input

(labels) for DNNs,³⁵ which degenerates the search space into a slice of the free-form continuous design space. Recent breakthrough on physics-driven adjoint-based networks^{36–38} overcomes the issues of discretization and degeneracy of the search space. However, more transparent and generalized machine learning frameworks with low training load for global optimization of non-convex problems still need to be developed for high-dimensional thermal photonic metasurface design. Another challenge is the poor manufacturability of the complex geometries of meta-atoms derived from these NN-based frameworks. To date, high-dimensional metasurfaces designed by NN and machine learning algorithms have rarely been experimentally demonstrated, owing to the complex shapes with highly nonuniform fill fractions, large radii of curvatures, and high aspect ratios.^{39–45} Practical fabrication constraints, such as the geometry complexity, the aspect ratio as well as the compatibility with the semiconductor foundry should be taken into consideration in the high-dimensional metasurface design.

In this work, we propose a transparent, explainable deep-learning Bayesian optimization (E-DeepBO) framework and a library of manufacturable high-dimensional metasurfaces. We visualize the deep-learning optimization process through pattern recognition and identify the sub-space key features of the high-dimensional metasurfaces, providing physics insights of the strong light-matter interaction across different bandwidths and thermal photonic design requirements. We showcase the applicability of the framework and the library by designing and experimentally realizing high-dimensional metasurfaces with different spectral bandwidths, i.e., a broadband selective solar absorber (SSA) and a narrowband thermophotovoltaic emitter (TE). Our work provides an explainable deep-learning photonic design platform with manufacturability and generality.

Figure 1 shows the schematic pipeline of the proposed E-DeepBO framework, which can simultaneously realize forward prediction from the given designs and inverse retrieval of the possible designs from the required optical responses. In the E-DeepBO, a visualized, predictive posterior distribution is generated by a DNN with Bayesian linear regression (BLR) applied to its last hidden layer, marginalizing only the output weights. The DNN-BLR significantly eases the training load and enables global optimization with balanced exploration and exploitation. As shown in Figs. 1(a) and 1(b), the meta-atom under investigation is a sandwiched structure that is composed of a continuous metallic ground plane, a dielectric spacer, and a top metallic resonator. The meta-atom is described by the feature vector $[h, d, a_1, b_1, a_2, b_2, a_3, b_3, a_4, b_4, a_5, b_5, a_6, b_6, a_7, b_7]$. Parameter a_i ($i = 1, 2, \dots, 7$) ranging from 0 to 500 nm continuously, denotes the width of each tungsten metallic resonator, while b_i ($i = 1, 2, \dots, 7$) with the same range denotes the width of the gap separating the neighboring tungsten metallic resonators. The first layer is a superposition of multi-fold tungsten metallic resonators, with the meta-atom periodicity continuously varied by the sum of a_i and b_i . In this work, we set the upper limit of the superposition as 7 for demonstration. The height of the first layer is denoted by h , which ranges from 0 to 300 nm continuously. Parameter d denotes the thickness of the SiO₂ dielectric spacer, ranging from 0 to 3000 nm continuously, forming the second layer under the multi-fold tungsten metallic resonators. The bottom layer is an opaque tungsten substrate. All the parameters of each possible candidate of the quasi-3D metasurface are represented by a 2D unit cell based on the symmetries of two orthogonal polarizations (Fig. S1). The entire design space is continuous. Yet, if we regard 1 nm

as the discrete unit, a design space with $500^{14} \times 300 \times 3000 \approx 10^{43}$ candidates in total is formed.

The required optical responses and bandwidths for the selective solar absorber (SSA) and the thermal emitter (TE) are vastly different. The SSA requires resonant coupling across a broad bandwidth range (0.4–4.0 eV) to achieve near-perfect absorption over the entire solar irradiance. The figure of merit (FOM) of the SSA is the solar-thermal efficiency (STE), which is defined as

$$STE = \frac{C \int_{\text{solar}} I_{\text{solar}}(\lambda) \alpha(\lambda) d\lambda - \int_{\text{solar}} I_{\text{BB}}(\lambda) \varepsilon(\lambda) d\lambda}{C \int_{\text{solar}} I_{\text{solar}}(\lambda) d\lambda}, \quad (1)$$

where C is the solar concentration number, $I_{\text{solar}}(\lambda)$ is the wavelength-dependent solar irradiation intensity of one sun, $\alpha(\lambda)$ is the wavelength-dependent absorption of the metasurface, which is equal to the emissivity $\varepsilon(\lambda)$ at the corresponding wavelength λ , and $I_{\text{BB}}(\lambda)$ is the blackbody radiation intensity at the operating temperature. The TE requires near-perfect emissivity over a tailored narrow bandwidth corresponding to the bandgap of the InGaAs photovoltaic cell (0.55–0.75 eV). The FOM of the TE is the spectral efficiency (SE), which is defined as

$$SE = \frac{\int_0^{\lambda_{\text{bandgap}}} bb(\lambda) \varepsilon(\lambda) d\lambda \frac{\lambda}{\lambda_{\text{bandgap}}}}{\int_0^{\infty} bb(\lambda) d\lambda}, \quad (2)$$

where λ_{bandgap} is the wavelength corresponding to the bandgap of the InGaAs cell (0.55 eV), $\varepsilon(\lambda)$ is the emissivity of the designed metasurface at the wavelength λ , and $bb(\lambda)$ is the intensity of the blackbody radiation at the working temperature (1673 K) of the TE.

As shown in Fig. 1(c), the DNN in the E-DeepBO framework is initialized by training from a randomly probed data with the size of 50 as *a priori*, without specific domain knowledge. The training takes only a few minutes. The mapping between the feature vector and the FOM is probed by finite-difference time-domain (FDTD) Maxwell solver (see supplementary material Note S1).⁴⁶ The DNN is used to perform the regression task. The BLR algorithm performs a probabilistic linear regression to the last hidden layer of the trained DNN and predicts *a posteriori* distribution of the FOM over the entire design space (see the supplementary material). BLR marginalizes only the output weights of the DNN and utilizes a point of interest (POI) algorithm as the sampling function, resulting in adaptive basis regression which only scales linearly with the number of probing (Fig. S2). The DNN-BLR is a scalable surrogate model with balanced exploration (the highest uncertainty) and exploitation (the highest predicted value). The optimal design predicted by the DNN-BLR is then probed by the FDTD Maxwell solver. The probed mapping is appended to the training set *a priori*, which updates *a posteriori* distribution of the DNN-BLR. The procedure loops until a satisfied design is eventually found. The E-DeepBO algorithm is highly efficient for such an astronomical continuous design space. The optimization process takes *ca.* 20 h on a moderate desktop workstation with 56-Core 3.2 GHz CPU and 128 GB memory, which is orders of magnitude faster than the previously reported BO-based and DNN-based optimization.^{47–49}

Different from the conventional DNN-based surrogate models, the DNN-BLR outputs a distribution of the regression results rather than a fixed value, which could provide more possibilities for exploration when sampling. We visualize the DNN-BLR through partial

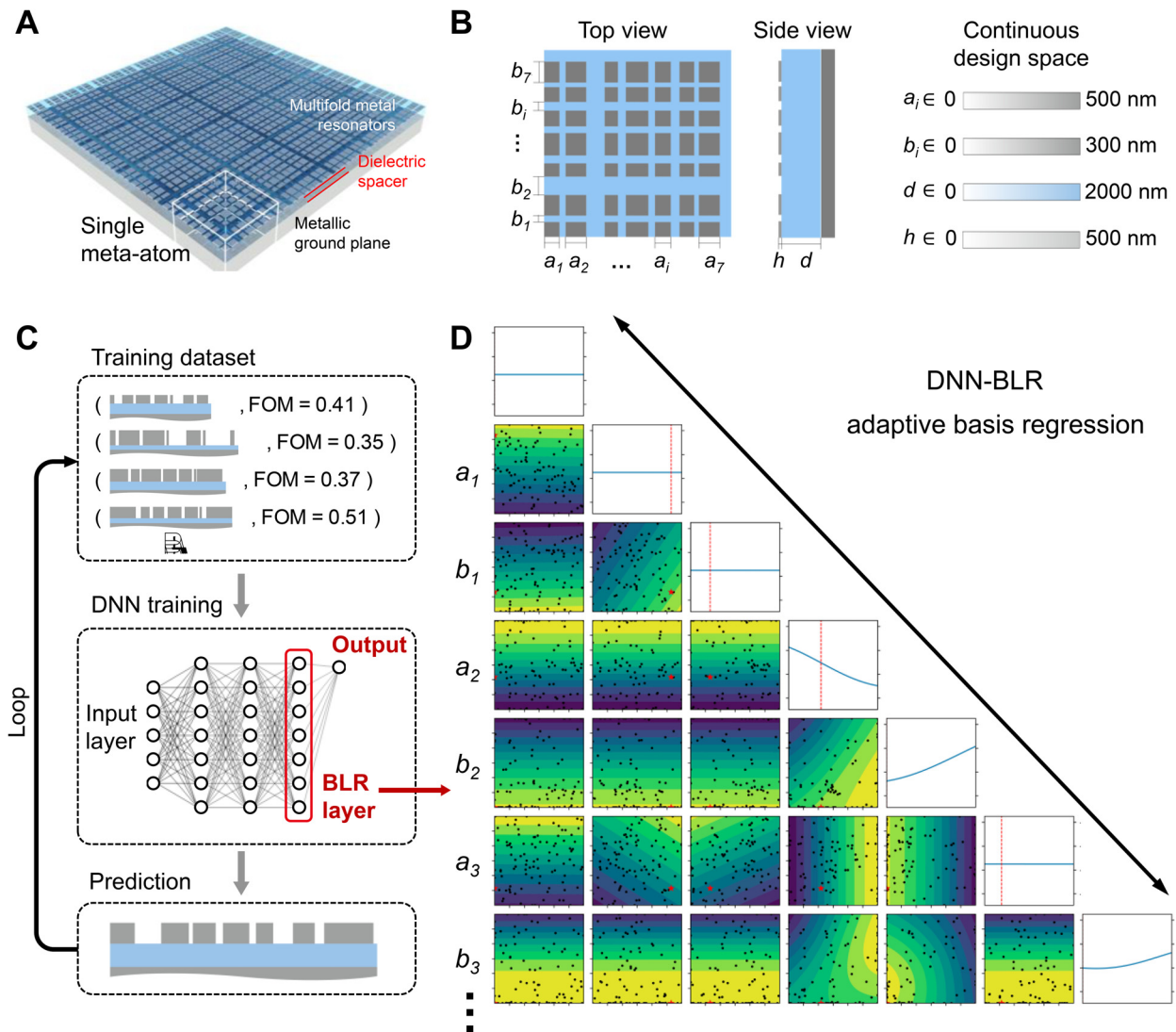


FIG. 1. Design pipeline of E-DeepGO. (a) The quasi-3D illustration of the sandwich-structured metasurface working in reflective configuration, which consists a continuous metallic ground plane, a dielectric spacer, and a top metallic resonator. (b) The continuous design space of the meta-atom unit cell. (c) The E-DeepBO framework. The initial training dataset for the DNN contains 50 geometry-FOM mappings. BLR is applied to the last hidden layer of the DNN, which predicts *a posteriori* distribution of the FOM over the entire design space. (d) Partial visualization of adaptive basis regression of six dimensions of the design space by the DNN-BLR. The full visualization of the 16-dimensional design space is given in Fig. S3.

dependence analysis (see Methods). While conventional DNN requires heavy training load and generates only isolated predictions for sampling, the DNN-BLR generates a distribution of the predictions with posterior mean and variance [Fig. 1(d)]. The distribution of predictions not only significantly eases the training load but also enables global optimization through an acquisition function balancing the exploitation (the highest posterior mean) and exploration (the highest variance). The relationship between variables of different dimensions within the predicted *a posteriori* distribution could also be extracted to obtain global perspectives on the entire design space and unfold the black-box of the DNN-based optimization. Meanwhile, the E-DeepBO framework enables the incorporation of the prior information on the

FOM and the search space, thus further reducing the training load of the DNN-BLR through closed loop.

We further carry out pattern recognition (PR) on the 16-dimensional design space using unsupervised machine learning (see Methods) to obtain global perspectives on the optimization process and physics insights of the metasurfaces. Since the meta-atom is periodic, a cyclic permutation on a_i and b_i gives exactly the same design. To make sure the parameters in PR are physically meaningful, the feature vectors are cyclically permuted such that the largest a_i is in the position of a_1 before PR, while the positions of h and d remain the same. The regulated feature vector is denoted by $[h, d, a'_1, b'_1, a'_2, b'_2, \dots, a'_7, b'_7]$. To explain the dynamic learning process, PR is performed on

the search dataset filtered by different FOM thresholds. Figure 2 shows the PR result of the TE metasurface as a demonstration-of-concept. The spectral efficiency threshold ranges from 0.52, covering 99.20% of the searched dataset, to 0.70, covering 37.23% of the

searched dataset. The full-threshold PR is provided in Fig. S4. The first and the third columns in Fig. 4 show the projection of the filtered datasets on the plane spanned by the first (x-axis) and second (y-axis) principal components. The second and the fourth columns show the PR

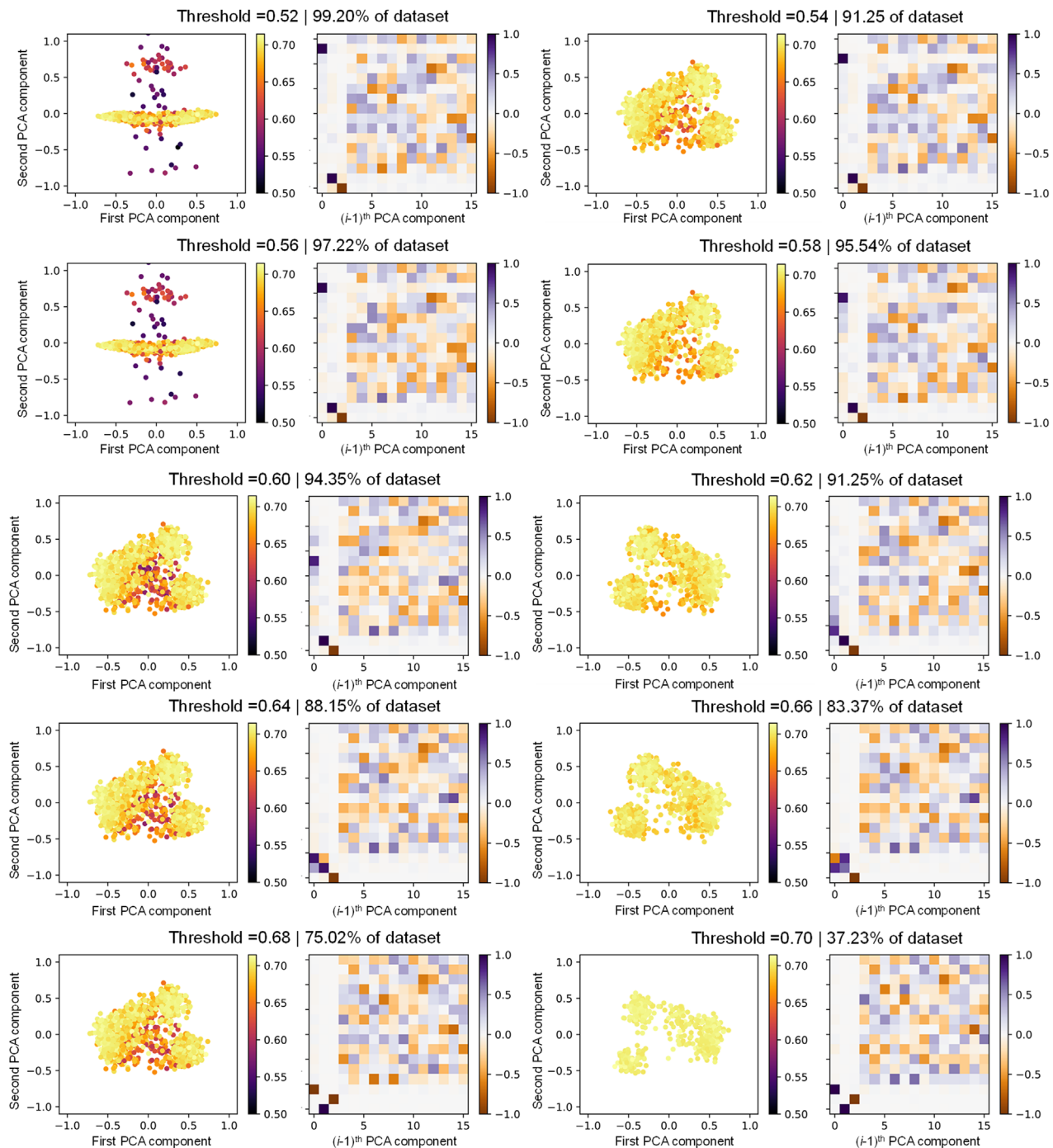


FIG. 2. Visualization of the optimization process of the TE through pattern recognition on the search dataset. The spectral efficiency threshold ranges from 0.52, which covers 99.20% of the entire search dataset, to 0.70 which covers 37.23% of the entire search dataset. The full-threshold visualization is provided in supplementary material Fig. S4.

components of each chosen dataset, in which each row symbolizes a PR component (the i th row corresponds to the i th principal component).

When the PR is performed on the 99.20% of the search dataset, the data points distribute in a broad range, which demonstrates sufficient exploration over the entire design space. According to the range set of the parameters, if the dataset is chosen uniformly, the variance in the d direction will be the largest, while the co-variance in a'_1 and b'_1 is supposed to be the least. The result of PR shows that the component with the largest variance is the direction of d , while the components with the least two variances are the directions of a'_1 and h . The order of variances calculated by the range setting agrees with the order of the principal components. The dataset is composed with a wide range of low-efficiency points and a cluster of high-efficiency points, demonstrating a balance between exploration and exploitation.

At a higher FOM threshold, the variance in the d direction becomes lower. Meanwhile, the variance along a'_1 surpasses h to be the least component. When the FOM threshold further increases to 0.70,

the three components with the least variance become a'_1 , h , and d . This means that the distribution of the high-FOM points along a'_1 , h , and d directions is narrow, indicating a'_1 , h , and d are the most critical parameters of the TE metasurface. Therefore, the performance of the TE metasurface is the most sensitive to the width and height of the largest tungsten resonator, which is the key to excite the surface plasmon polaritons [highlighted by a white-dashed box in Fig. 3(c)], as well as the thickness of the SiO₂ dielectric space, which is the key to excite the magnon polaritons [highlighted by a white-dashed box in Fig. 2(c)].

The feature vectors of the optimal metasurfaces for the SSA and the TE after 1400 optimization loops are [114, 41, 267, 169, 294, 128, 91, 70, 257, 450, 248, 245, 189, 74, 140, 267] and [54, 761, 302, 119, 416, 356, 252, 144, 442, 118, 316, 153, 300, 78, 406, 221], respectively. The optimized continuous-space feature vectors are truncated into integers to embody physically meaningful structures. Figure 3(a) shows the electric and magnetic field enhancement of the optimal SSA at different wavelengths. The broadband near-perfect absorption is realized

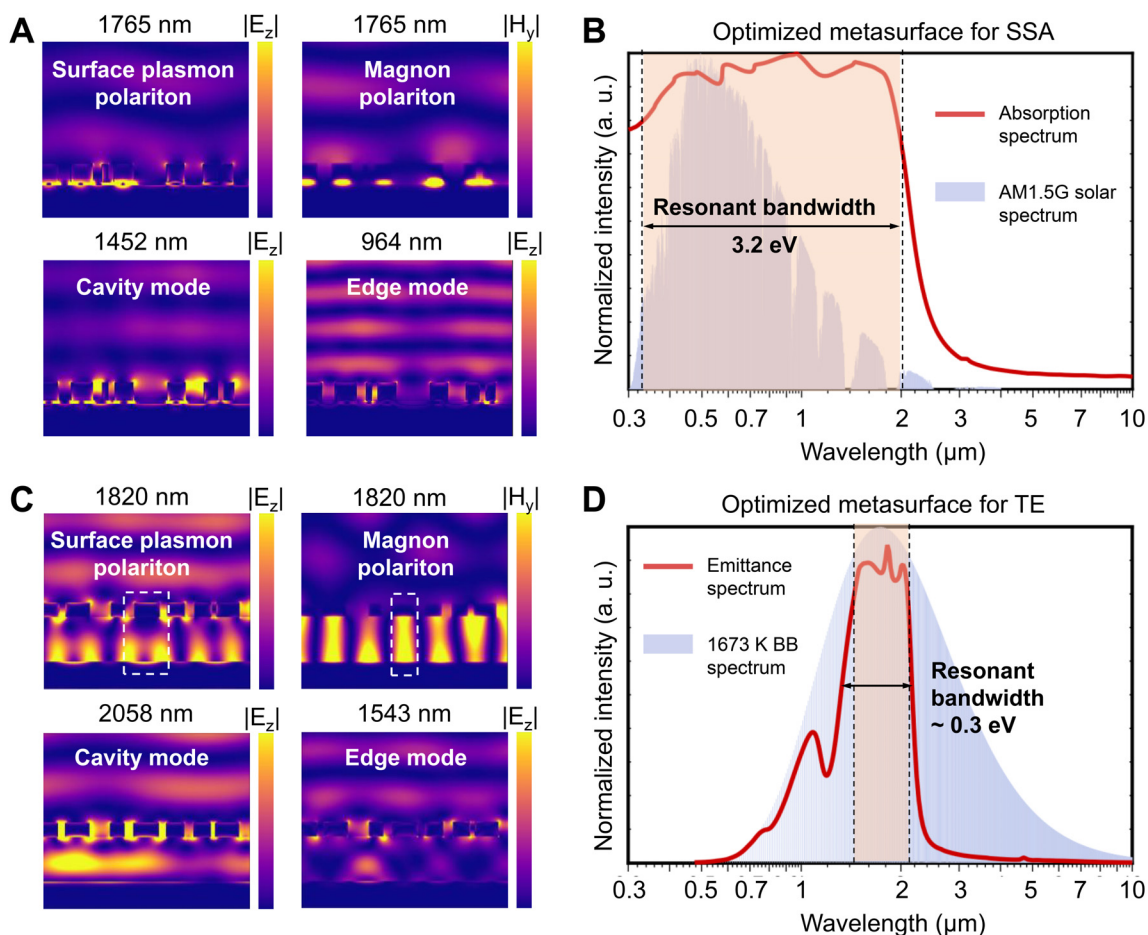


FIG. 3. Light-matter interaction of the designed SSA and TE. (a) Electric field distribution at the wavelengths of 1765, 1452, and 964 nm, as well as magnetic field distribution at the wavelength of 1765 nm for the designed SSA. (b) FDTD-calculated optical absorption of the SSA from 0.3 to 10 μm . The AM1.5G solar irradiation spectrum is shown as background. (c) Electric field distribution at the wavelengths of 1820, 2058, and 1543 nm, as well as magnetic field distribution at the wavelength of 1820 nm for the designed TE. (d) FDTD-calculated thermal emittance of the TE from 0.3 to 10 μm . The 1673 K blackbody radiation spectrum is shown as background.

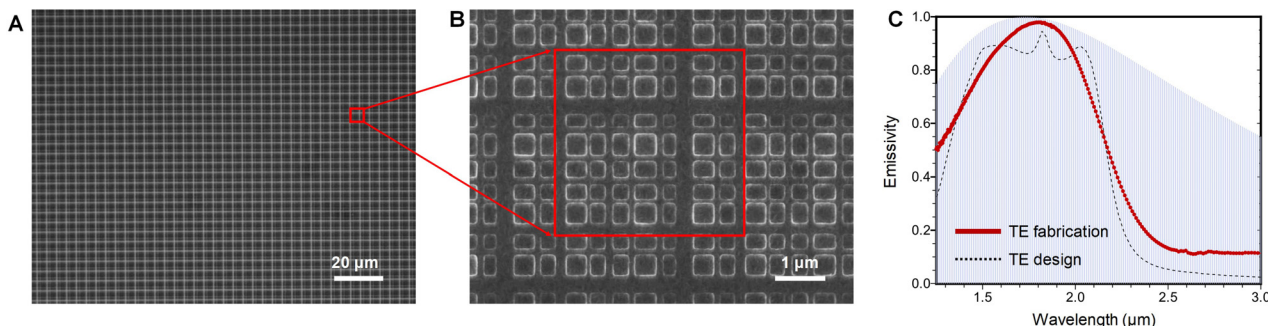


FIG. 4. Fabrication and characterization of the TE. (a) Optical microscopic image of the fabricated TE. (b) SEM image of an individual superimposed meta-atom of the fabricated TE. (c) Experimental absorption spectra of the fabricated TE measured by Fourier-transformed infrared spectroscopy.

by different strong light–matter interaction regimes. Notably, the incidence at 1765 nm wavelength excites both surface plasmon polariton and magnon polariton within the dielectric spacer, as, respectively, demonstrated by the electric and magnetic field enhancement in Fig. 3(a). The 1452 nm wavelength incidence excites the cavity mode with the electric field enhancement between the metallic resonators. For the incidence of 964 nm wavelength and below, the field enhancement is transitioned to the edge mode which has a broad light–matter interaction bandwidth but relatively weak intensity. The intensity could be further increased using an anti-reflection coating.⁵⁰ As shown in Fig. 3(b), the total resonant bandwidth of the SSA is 3.2 eV. The absorption spectrum of the optimal SSA is near perfect over the entire solar irradiance and is quenched sharply in the thermal radiation wavelength range, resulting in a high STE of 95%. As shown in Fig. 3(c), the field enhancement mapping for the optimal TE also demonstrates the superposition of the surface plasmon polariton, magnon polariton, cavity mode, and edge mode, excited by the incidence at 1820, 2058, and 1543 nm, respectively. The total resonant bandwidth of the TE is tailored to 0.3 eV [Fig. 3(d)]. The spectral efficiency of the optimal TE is 0.71, which is the highest efficiency for the TE metasurface design reported so far.⁵¹ The discovery of the fourfold superposition of light–matter interaction through the V-DeepBO framework, i.e., the superposition of the surface plasmon polariton, magnon polariton, cavity mode, and edge mode, presents a significant progress in photonic design.

We fabricate the TE using electron-beam lithography (see Methods) as demonstration. Figures 4(a) and 4(b) show the optical microscopy and the scanning electron microscopy (SEM) images of the fabricated TE. The fabricated TE metasurface is uniform and matches with the design over a large area. We measure the absorption spectra of the fabricated TE using FT-IR spectroscopy. The absorption spectrum of the fabricated TE has sharp transition from high to low absorption near the cutoff wavelength of 2254 nm, which matches well with the design. The experimental results demonstrate the sound manufacturability of the metasurfaces designed by E-DeepBO to realize multifunctional metasurface devices.

The E-DeepBO framework developed in our work unfolds the black-box NN approximator with very small training load and realized efficient global optimization of fabrication-friendly, high-dimensional metasurfaces that generalize across different light–matter interaction bandwidths. Through E-DeepBO, high-efficiency broadband SSA and narrowband TE are realized with the superposition of surface plasmon

polariton, magnon polariton, cavity mode, and edge mode. The global optimization process of the high-dimensional metasurfaces is visualized through pattern recognition based unsupervised machine learning. The sub-space key features of the high-dimensional design space are identified, which could inspire physical insights for the design of complex metasurfaces. Our work provides an explainable deep-learning global optimization platform with high scalability, high efficiency, and generality for data-intensive photonic design and light–matter interaction regime discovery.

See the [supplementary material](#) for computational and fabrication details, the FOM difference between 2D and quasi-3D FDTD calculations based on the symmetries of orthogonal polarizations, computational time per optimization loop for E-DeepBO and conventional GP-based BO, the full-dimensional visualization of adaptive basis regression by the DNN-BLR, and the full-threshold visualization of the optimization process by PR on the E-DeepBO search dataset of the TE.

This work is sponsored by the National Natural Science Foundation of China (52371139), Consulting Decision-Making Project (JCZXSJB2024-07), Zhiyuan Future Scholar Program, and Faculty Startup Funding (WF220405012) from Shanghai Jiao Tong University. This research made use of shared facilities of Zhiyuan Innovative Research Center (ZIRC) and Instrumental Analysis Center at SJTU.

AUTHOR DECLARATIONS

Conflict of Interest

The authors have no conflicts to disclose.

Author Contributions

Jintao Chen and Zihan Zhang contributed equally to this work.

Jintao Chen: Data curation (equal); Investigation (equal); Visualization (equal); Writing – original draft (equal). **Zihan Zhang:** Data curation (equal); Investigation (equal); Visualization (equal); Writing – original draft (equal). **Zhequn Huang:** Funding acquisition (supporting); Project administration (supporting); Supervision (supporting); Writing – review & editing (supporting). **Kehang Cui:** Conceptualization (lead); Data curation (equal); Funding acquisition

(lead); Investigation (supporting); Project administration (lead); Supervision (lead); Writing – original draft (lead); Writing – review & editing (lead).

DATA AVAILABILITY

The data that support the findings of this study are available within the article and its [supplementary material](#).

REFERENCES

- ¹Y. Li, W. Li, T. Han, X. Zheng, J. Li, B. Li, S. Fan, and C.-W. Qiu, *Nat. Rev. Mater.* **6**, 488–507 (2021).
- ²S. Fan, *Joule* **1**, 264–273 (2017).
- ³D. G. Baranov, Y. Xiao, I. A. Nechepurenko, A. Krasnok, A. Alù, and M. A. Kats, *Nat. Mater.* **18**, 920–930 (2019).
- ⁴A. M. Shaltout, V. M. Shalaev, and M. L. Brongersma, *Science* **364**, eaat3100 (2019).
- ⁵S. Yang, M. Liu, C. Zhao, S. Fan, and C.-W. Qiu, *Nat. Photonics* **18**, 412–424 (2024).
- ⁶X. Li, Z. Wen, D. Zhou, J. Zhang, Y. Sun, H. Xu, X. Shi, D. Cao, Y. Zhang, N. Dai, F. Liu, and J. Hao, *Cell Rep. Phys. Sci.* **4**, 101687 (2023).
- ⁷J. Zhou, B. Wang, and C. Zhao, *IEEE Sens. J.* **24**, 20468–20475 (2024).
- ⁸J. Meng, S. Balendhran, Y. Sabri, S. K. Bhargava, and K. B. Crozier, *Microsyst. Nanoeng.* **10**, 74 (2024).
- ⁹A. Lochbaum, Y. Fedoryshyn, A. Dorodny, U. Koch, C. Hafner, and J. Leuthold, *ACS Photonics* **4**, 1371–1380 (2017).
- ¹⁰A. Leitis, M. L. Tseng, A. John-Herpin, Y. S. Kivshar, and H. Altug, *Adv. Mater.* **33**, 2102232 (2021).
- ¹¹Q. Chu, F. Zhang, Y. Zhang, T. Qiao, S. Zhu, and H. Liu, *Nanophotonics* **11**, 4263–4271 (2022).
- ¹²F. Bao, X. Wang, S. H. Sureshbabu, G. Sreekumar, L. Yang, V. Aggarwal, V. N. Boddeti, and Z. Jacob, *Nature* **619**, 743–748 (2023).
- ¹³X. Wang, Z. Yang, F. Bao, T. Sentz, and Z. Jacob, *Optica* **11**, 73–80 (2024).
- ¹⁴D. Thompson, L. Zhu, E. Meyhofer, and P. Reddy, *Nat. Nanotechnol.* **15**, 99–104 (2020).
- ¹⁵J. W. Lim, A. Majumder, R. Mittapally, A.-R. Gutierrez, Y. Luan, E. Meyhofer, and P. Reddy, *Nat. Commun.* **15**, 5584 (2024).
- ¹⁶Y. Li, Y. Dang, S. Zhang, X. Li, Y. Jin, P. Ben-Abdallah, J. Xu, and Y. Ma, *Phys. Rev. Appl.* **20**, 024061 (2023).
- ¹⁷H. Zhu, Q. Li, C. Zheng, Y. Hong, Z. Xu, H. Wang, W. Shen, S. Kaur, P. Ghosh, and M. Qiu, *Light Sci. Appl.* **9**, 60 (2020).
- ¹⁸H. Zhu, Q. Li, C. Tao, Y. Hong, Z. Xu, W. Shen, S. Kaur, P. Ghosh, and M. Qiu, *Nat. Commun.* **12**, 1805 (2021).
- ¹⁹W. Xi, Y.-J. Lee, S. Yu, Z. Chen, J. Shiomi, S.-K. Kim, and R. Hu, *Nat. Commun.* **14**, 4694 (2023).
- ²⁰R. Hu, W. Xi, Y. Liu, K. Tang, J. Song, X. Luo, J. Wu, and C.-W. Qiu, *Mater. Today* **45**, 120–141 (2021).
- ²¹B. Qin, Y. Zhu, Y. Zhou, M. Qiu, and Q. Li, *Light Sci. Appl.* **12**, 246 (2023).
- ²²A. LaPotin, K. L. Schulte, M. A. Steiner, K. Buznitsky, C. C. Kelsall, D. J. Friedman, E. J. Tervo, R. M. France, M. R. Young, A. Rohskopf, S. Verma, E. N. Wang, and A. Henry, *Nature* **604**, 287–291 (2022).
- ²³D. Fan, T. Burger, S. McSherry, B. Lee, A. Lenert, and S. R. Forrest, *Nature* **586**, 237–241 (2020).
- ²⁴E. J. Tervo, R. M. France, D. J. Friedman, M. K. Arulanandam, R. R. King, T. C. Narayan, C. Luciano, D. P. Nizamian, B. A. Johnson, A. R. Young, L. Y. Kuritzky, E. E. Perl, M. Limpinsel, B. M. Kayes, A. J. Ponec, D. M. Bierman, J. A. Briggs, and M. A. Steiner, *Joule* **6**, 2566–2584 (2022).
- ²⁵B. Roy-Layinde, J. Lim, C. Arneson, S. R. Forrest, and A. Lenert, *Joule* **8**, 2135–2145 (2024).
- ²⁶Z. Huang, C. Cao, Q. Wang, H. Zhang, C. E. Owens, A. J. Hart, and K. Cui, *Nano Lett.* **22**, 8526–8533 (2022).
- ²⁷A. Sakurai, K. Yada, T. Simomura, S. Ju, M. Kashiwagi, H. Okada, T. Nagao, K. Tsuda, and J. Shiomi, *ACS Cent. Sci.* **5**, 319–326 (2019).
- ²⁸Q. Wang, Z. Huang, J. Li, G.-Y. Huang, D. Wang, H. Zhang, J. Guo, M. Ding, J. Chen, Z. Zhang, Z. Rui, W. Shang, J.-Y. Xu, J. Zhang, J. Shiomi, T. Fu, T. Deng, S. G. Johnson, H. Xu, and K. Cui, *Nano Lett.* **23**, 1144–1151 (2023).
- ²⁹Z. Fan, C. Qian, Y. Jia, M. Chen, J. Zhang, X. Cui, E.-P. Li, B. Zheng, T. Cai, and H. Chen, *Phys. Rev. Appl.* **18**, 024022 (2022).
- ³⁰J. Zhang, C. Qian, Z. Fan, J. Chen, E. Li, J. Jin, and H. Chen, *Adv. Opt. Mater.* **10**, 2200748 (2022).
- ³¹Y. Jia, C. Qian, Z. Fan, T. Cai, E.-P. Li, and H. Chen, *Light Sci. Appl.* **12**, 82 (2023).
- ³²Y. Wang, Y. Zhu, Z. Cui, H. Jiang, K. Zhang, and X. Wang, *J. Opt. Soc. Am. B* **39**, 835–842 (2022).
- ³³B. Lou, J. A. Rodriguez, B. Wang, M. Cappelli, and S. Fan, *ACS Photonics* **10**, 1806–1812 (2023).
- ³⁴W. Ji, J. Chang, H.-X. Xu, J. R. Gao, S. Gröblacher, H. P. Urbach, and A. J. L. Adam, *Light Sci. Appl.* **12**, 169 (2023).
- ³⁵W. Ma, Y. Xu, B. Xiong, L. Deng, R.-W. Peng, M. Wang, and Y. Liu, *Adv. Mater.* **34**, 2110022 (2022).
- ³⁶J. Jiang and J. A. Fan, *Nano Lett.* **19**, 5366–5372 (2019).
- ³⁷M. Chen, R. Lupoiu, C. Mao, D.-H. Huang, J. Jiang, P. Lalanne, and J. A. Fan, *ACS Photonics* **9**, 3110–3123 (2022).
- ³⁸E. Gershnel, M. Chen, C. Mao, E. W. Wang, P. Lalanne, and J. A. Fan, *ACS Photonics* **10**, 815–823 (2023).
- ³⁹A. Ueno, H.-I. Lin, F. Yang, S. An, L. Martin-Monier, M. Y. Shalaginov, T. Gu, and J. Hu, *Nanophotonics* **12**, 3491–3499 (2023).
- ⁴⁰I. Tanrıover, D. Lee, W. Chen, and K. Aydin, *ACS Photonics* **10**, 875–883 (2023).
- ⁴¹R. P. Jenkins, S. D. Campbell, and D. H. Werner, *Nanophotonics* **10**, 4497–4509 (2021).
- ⁴²Z. Liu, D. Zhu, K.-T. Lee, A. S. Kim, L. Raju, and W. Cai, *Adv. Mater.* **32**, 1904790 (2020).
- ⁴³E. Khoram, X. Qian, M. Yuan, and Z. Yu, *Opt. Express* **28**, 7060–7069 (2020).
- ⁴⁴Y. Zhou, C. Mao, E. Gershnel, M. Chen, and J. A. Fan, *Laser Photonics Rev.* **18**, 2300988 (2024).
- ⁴⁵Y. Zhou, Y. Shao, C. Mao, and J. A. Fan, *J. Opt.* **26**, 055101 (2024).
- ⁴⁶A. F. Oskooi, D. Roundy, M. Ibanescu, P. Bermel, J. D. Joannopoulos, and S. G. Johnson, *Comput. Phys. Commun.* **181**, 687–702 (2010).
- ⁴⁷W. Ma, Z. Liu, Z. A. Kudyshev, A. Boltasseva, W. Cai, and Y. Liu, *Nat. Photonics* **15**, 77–90 (2021).
- ⁴⁸J. Jiang, M. Chen, and J. A. Fan, *Nat. Rev. Mater.* **6**, 679–700 (2020).
- ⁴⁹F. Pedregosa, G. Varoquaux, A. Gramfort, V. Michel, B. Thirion, O. Grisel, M. Blondel, P. Prettenhofer, R. Weiss, V. Dubourg, J. Vanderplas, A. Passos, D. Cournapeau, M. Brucher, M. Perrot, and É. Duchesnay, *J. Mach. Learn. Res.* **12**, 2825–2830 (2011); available at <http://jmlr.org/papers/v12/pedregosa11a.html>.
- ⁵⁰H. K. Raut, V. A. Ganesh, A. S. Nair, and S. Ramakrishna, *Energy Environ. Sci.* **4**, 3779–3804 (2011).
- ⁵¹T. Burger, C. Sempere, B. Roy-Layinde, and A. Lenert, *Joule* **4**, 1660–1680 (2020).

Supporting Information

Thermal emission modulation of fabrication-friendly, free-form metasurfaces via explainable deep-learning Bayesian optimization

Jintao Chen,^{1†} Zihan Zhang,^{2†} Zhequn Huang,³ Kehang Cui^{4*}

¹School of Electronic Information and Electrical Engineering, Shanghai Jiao Tong University, Shanghai 200240, China

²School of Mathematical Science, Shanghai Jiao Tong University, Shanghai 200240, China

³Zhiyuan Innovative Research Center, Shanghai Jiao Tong University, Shanghai 200240, China

⁴School of Materials Science and Engineering, Shanghai Jiao Tong University, Shanghai 200240, China

[†]These authors contribute equally to this work.

*Corresponding author: Kehang Cui, cuikeh@sjtu.edu.cn

Finite-difference time domain (FDTD) method

In each loop, the predicted point is probed by FDTD simulation. We use the MEEP package¹ to carry out the FDTD simulation. The optical properties of the materials are adopted from Rakic *et al*² using Lorentzian-Drude model. The FDTD simulation uses a transverse-magnetic mode Gaussian distributed source. The boundary conditions include periodic boundary condition as well as perfectly matched layers on top and bottom of the unit cell.

Visualized deep-learning Bayesian optimization (V-DeepBO) framework

The DNN in V-DeepBO is a fully connected feed-forward network, which has three layers with 50 neurons per layer. The activation function of the DNN is bounded tanh function.⁴⁹ No activation function is applied to the output layer. Instead, BLR is performed on the last hidden layer of the DNN, so that the outputs of the last hidden layer give a posterior predictive distribution of the target function, rather than isolated values predicted by the conventional DNNs. The posterior distribution $p(\mathbf{w}|\mathbf{t})$ of BLR is given by

$$\ln p(\mathbf{w}|\mathbf{t}) = -\frac{\beta}{2} \sum_{n=1}^N \{t_n - \mathbf{w}^T \phi(x_n)\}^2 - \frac{\alpha}{2} \mathbf{w}^T \mathbf{w} + \text{const.} \quad (\text{S1})$$

where α specifies the variance of the prior for the weight vector \mathbf{w} ; β defines the inverse of the noise; \mathbf{t} is the target vector; x_n is the input; $\phi(x)$ is the basis function. The first term is the sum of log likelihood, and the second term is the log of the prior as a function of \mathbf{w} . The L-BFGS-B algorithm is utilized to maximize the likelihood of the Expected Improvement (EI) acquisition function in each loop.

Pattern recognition (PR)

The PR process transforms high-dimensional, complex data vectors into a lower-dimensional form while retaining the original data's variance as much as possible. For a given feature matrix X composed of n feature vectors, the centered data matrix \widehat{X} is first calculated by subtracting the mean vector μ . Then, the covariance matrix Σ describing how each feature vector relates to every other is calculated by:

$$\Sigma = \frac{1}{n-1} \widehat{X}^T \widehat{X} \quad (\text{S2})$$

Then a subset of the eigenvectors (principal components) is selected from Σ based on the variance. The eigenvalues indicate the amount of variance explained by each eigenvector, and are sorted in a descending order to screen the top k eigenvectors. k is a hyper-parameter and is chosen based on the desired degree of dimensionality reduction. Finally, the selected principal components are used to transform the original data into a new coordinate system:

$$\bar{X} = \hat{X}V_k \quad (\text{S3})$$

where V_k contains the top k eigenvectors. The transformed data \bar{X} represents the original data in a lower-dimensional space with the most important features retained.

Fabrication and characterization

The Si wafer substrate was cleaned by the RCA process followed by plasma cleaning. A 100 nm-thick tungsten film and a 761 nm-thick SiO_2 were sequentially deposited on the Si wafer substrate by sputtering. A 360 nm-thick positive electron beam resist (ZEP) was then deposited by spin coating. Electron beam lithography was carried out to obtain the designed pattern on the resist. A 54 nm-thick tungsten film was again deposited on the pattern. The structure was eventually obtained through a solution-based lift-off process. The total size of the sample is 1 mm x 1mm. The microscale surface morphology of the fabricated structure was observed by Zeiss Gemini SEM. The reflectance spectrum was measured by Nicolet iN10 MX Infrared Imaging Microscope (Thermo Fisher) with the liquid nitrogen-cooled MCT-A detector.

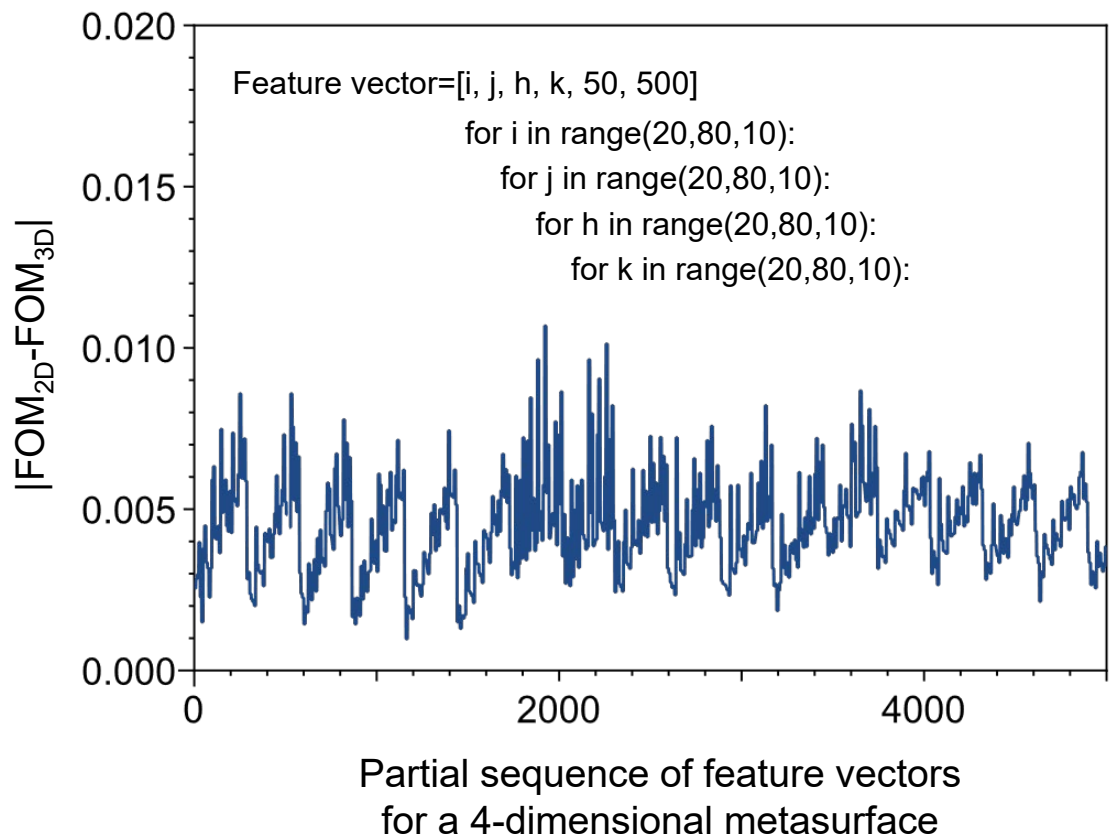


Figure S1. The FOM difference between 2D and quasi-3D FDTD calculations based on the symmetries of orthogonal polarizations. The difference is negligible (less than 1%), thus we adopt 2D calculation in this study for simplicity.

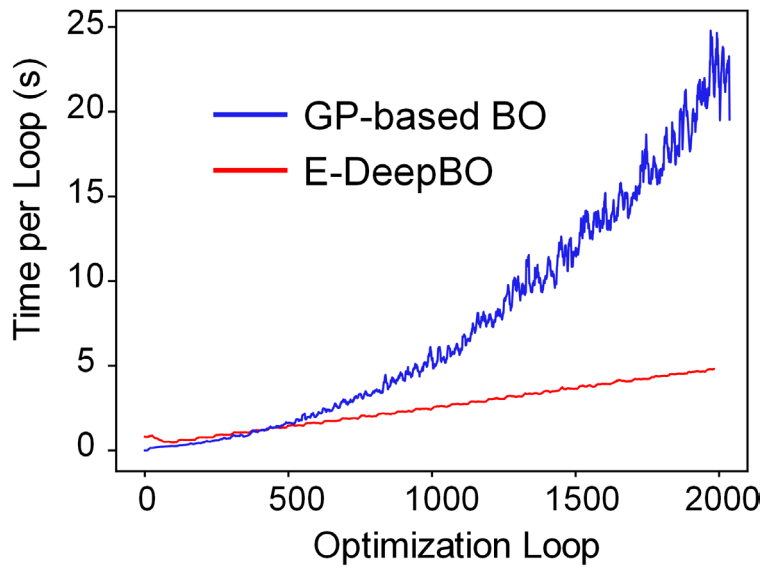


Figure S2. Computational time per optimization loop for E-DeepBO and conventional GP-based BO.

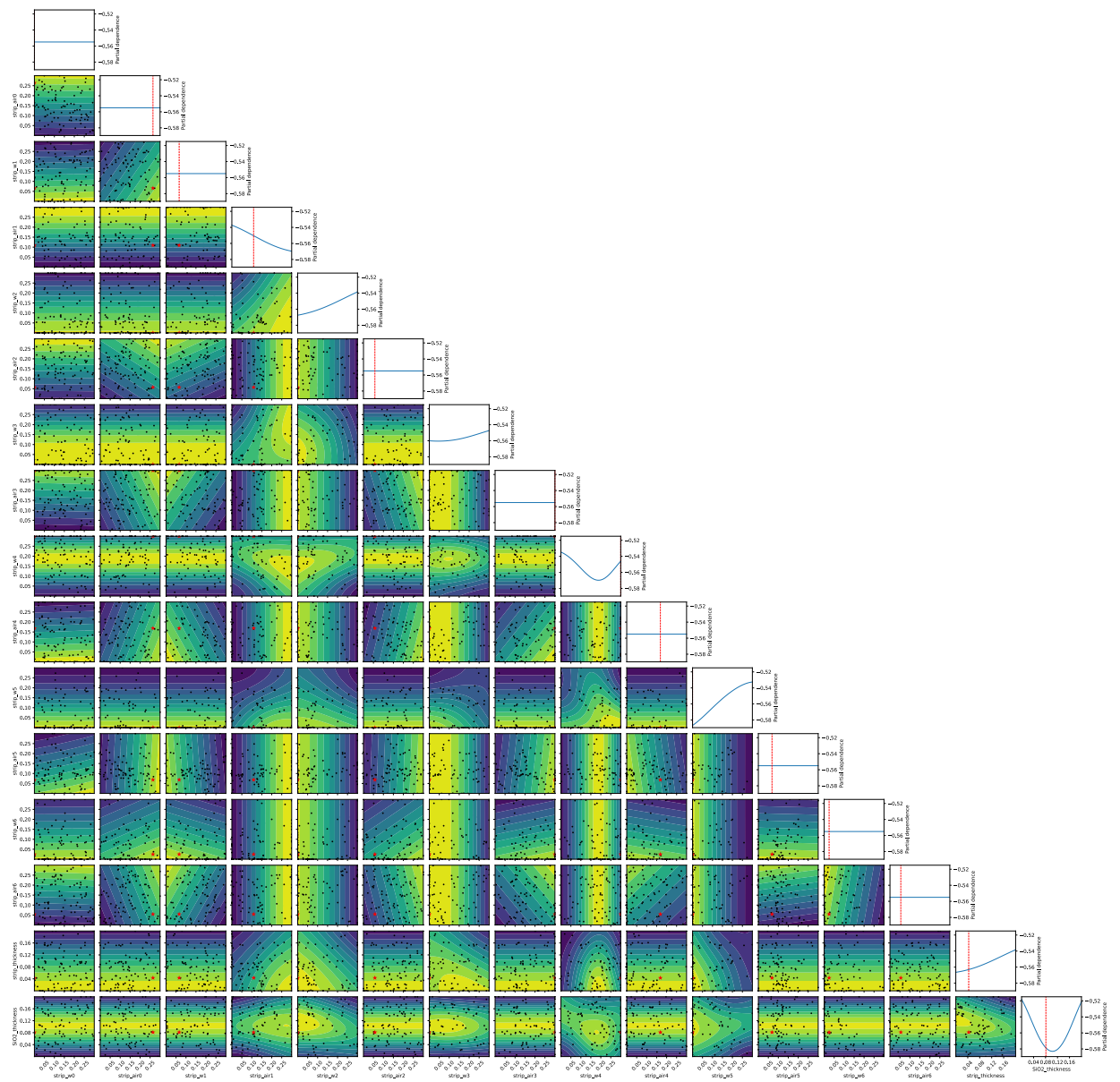


Figure S3. Full visualization of adaptive basis regression of the 16-dimensional design space by the DNN-BLR.

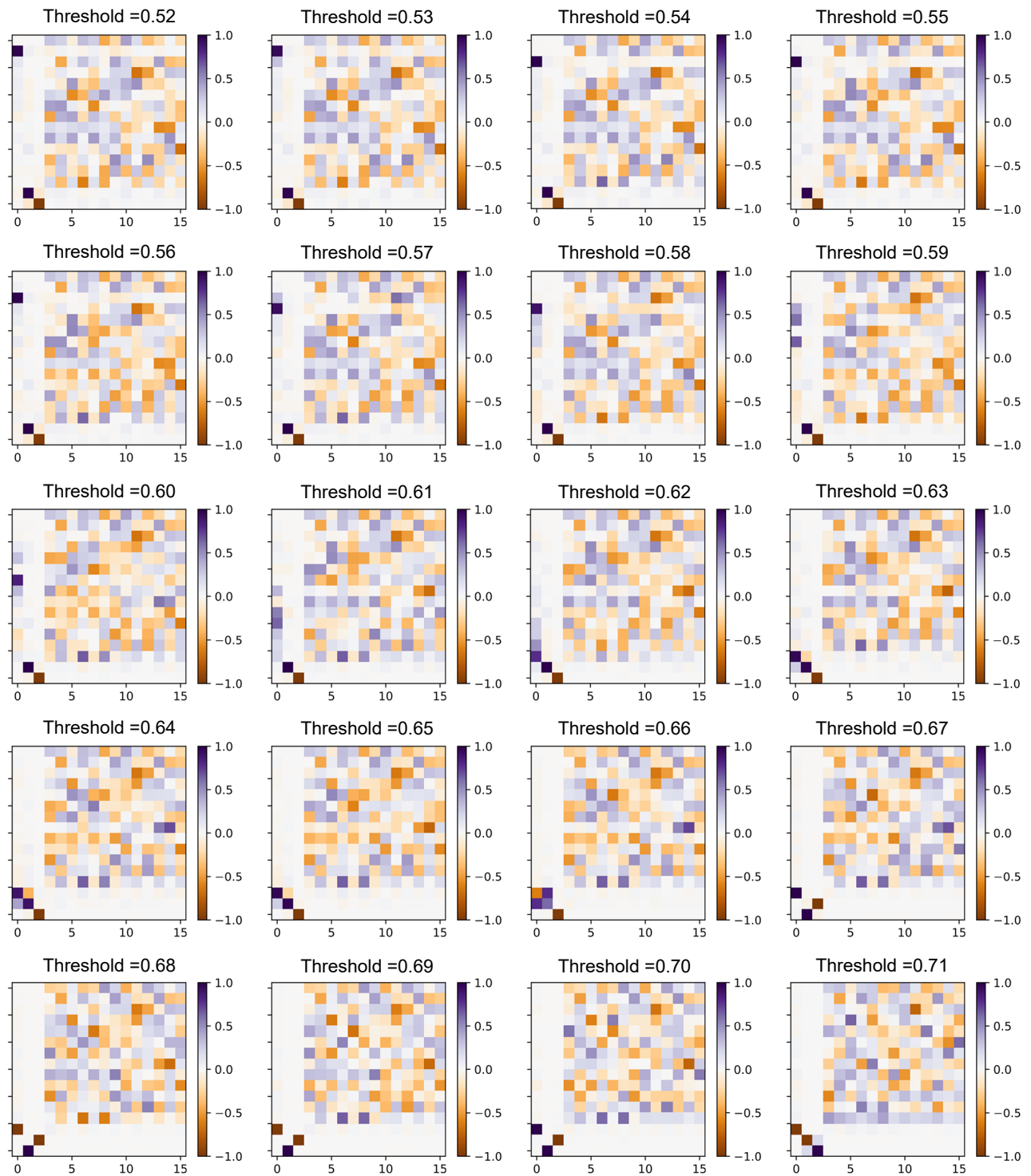


Figure S4. Full-threshold visualization of the optimization process by pattern recognition (PR) on the E-DeepBO search dataset of the TE.

Reference

- [1] Oskooi, A. F.; Roundy, D.; Ibanescu, M.; Bermel, P.; Joannopoulos, J. D.; Johnson, S. G., Meep: A flexible free-software package for electromagnetic simulations by the FDTD method. *Computer Physics Communications* **2010**, *181* (3), 687-702.
- [2] Rakic, A. D.; Djurisic, A. B.; Elazar, J. M.; Majewski, M. L., Optical properties of metallic films for vertical-cavity optoelectronic devices. *Appl Opt* **1998**, *37* (22), 5271-83.